Millimeter-Size All-inorganic Perovskite Crystalline Thin Film Grown by Chemical Vapor Deposition

Yuan Zhou, Kasun Fernando, Juanyong Wan, Fangze Liu, Shreetu Shrestha, Jeremy Tisdale, Chris J. Sheehan, Andrew C. Jones, Sergei Tretiak, Hsinhan Tsai,* Huihui Huang,* and Wanyi Nie*

The chemical vapor deposition (CVD) method is a dry approach that can produce high quality crystals and thin films at large scale which can be easily adapted by industry. In this work, CVD technology is employed to grow high quality, large size all-inorganic cesium lead bromide perovskite crystalline film for the first time. The obtained films have millimeter size crystalline domains with high phase purity. The growth kinetics are examined in detail by optical microscopy and X-ray diffraction. The deposition rate and growth temperature are found to be the key parameters allowing to achieve large scale crystal growth. The large crystalline grains exhibit exceptional optical properties including negligible Stokes shift and uniform photoluminescence over a large scale. This suggests a high degree of crystallinity free from internal strain or defects. A lateral diode within one large crystalline grain is further fabricated and significant photo-generated voltage and short circuit current are observed, suggesting highly efficient carrier transport and collections without scattering within the grain. This demonstration suggests that the CVD grown all-inorganic perovskite thin films enable a promising fabrication route suitable for photovoltaic or photo-detector applications.

1. Introduction

The discovery of high-quality semiconducting materials and the progress in their synthesis methods have played a vital role in recent opto-electronic device innovation. Halide perov-

Y. Zhou, J. Wan, Prof. H. Huang
School of Physics and Electronics
Hunan University
Hunan 410082, China
E-mail: huangh@hnu.edu.cn
Y. Zhou, Dr. K. Fernando, J. Wan, Dr. F. Liu, Dr. S. Shrestha, Dr. J. Tisdale, Dr. C. J. Sheehan, Dr. A. C. Jones, Dr. S. Tretiak, Dr. H. Tsai, Dr. W. Nie
Center for Integrated Nanotechnologies
Material Physics and Application Division
Los Alamos National Laboratory
Los Alamos, NM 87545, USA
E-mail: hsinhantsai@lanl.gov; wanyi@lanl.gov
Dr. S. Tretiak
Theoretical Division & Center for Integrated Nanotechnologies (CINT)
Los Alamos National Laboratory
Los Alamos, NM 87545, USA

The ORCID identification number(s) for the author(s) of this article can be found under https://doi.org/10.1002/adfm.202101058.

skites with a general formula of AMX_3, where A site is cations (Cs, CH_3NH_3, or $HC(NH_2)_2$), M is metal core (Ge, Sn, or Pb), and X is halides (Cl, Br, or I,), are an emerging class of semiconductors with extraordinary optoelectronic properties such as long carrier recombination lifetimes,[1] high mobilities,[2] and low defect densities,[3] rivaling that of other classical semiconductors. Importantly, the halides perovskites have other advantages like low cost and ease of fabrication in large scales that have thus far attracted intense research effort in recent years.[4] Among various perovskite structures, all-inorganic cesium lead halide ($CsPbX_3$) perovskite possess competitive properties particularly suitable for light-emitting diodes[5] and high-energy radiation detector.[6] Moreover, they are more tolerant to moisture and heat, thus presenting great advantages over their organic-inorganic hybrid counterparts which have environmental stability issues when operating under extreme environment.[7]

For high performance device applications, an efficacious and robust way of growing high-quality material is paramount. Most of the existing research and development of $CsPbX_3$ material growth are mainly focused on producing bulk single crystals[6a–c,8] or nano-structures.[5a,9] However, growing high quality cesium lead bromide perovskite ($CsPbBr_3$) thin films by solution methods met several challenges. On one hand, due to the complicated Cs–Pb–X phase diagram, undesired phases could often form that are detrimental to the opto-electronic properties. Besides, the phase purity can be affected by other factors such as the ratio of the precursors, the choice of solvent/antisolvent, and the growth temperature.[10] Moreover, the low solubility of CsBr in common organic solvents such as dimethylformamide and dimethyl sulfoxide (DMSO) results in stoichiometric imbalance limiting scalable crystal growth and can also lead to undesired phases such as Cs_4PbBr_6 or $CsPb_2Br_5$.[5b,6b,11] In addition, the solvent residue in the $CsPbBr_3$ crystal growth process when using solution method, causes persistent electronic defects in the crystal.[6a,b,8]

Owing to the high reproducibility and scalability, the chemical vapor deposition (CVD) has been widely utilized in industry for semiconductor fabrications. This method can be

**ADVANCED
SCIENCE NEWS**
www.advancedsciencenews.com

**ADVANCED
FUNCTIONAL
MATERIALS**
www.afm-journal.de

potentially used to address the above-mentioned challenges for $CsPbBr_3$ growth. As a solvent-free fabrication method, CVD method has been shown to be very effective for thin film morphology control and is able to minimize surface defects, which improve the material quality and stability. Moreover, it can avoid the solvent trapping issue during crystal growth process. Because of these advantages, pioneer works have demonstrated the high-quality all-inorganic $CsPbBr_3$ perovskite growth via CVD approach.[12] By carefully controlling the cooling rate and growth time, various $CsPbBr_3$ micro-morphologies with different phases, including microplates (cubic phase), pyramids (monoclinic phase), and microspheres (monoclinic phase), can be controllably synthesized.[13] Moreover, by tuning the deposition temperature, different micro-structures such as microwires (380 °C), microplates (340 °C), and triangular pyramids (300 °C) can be synthesized.[14] Interestingly, recent reports also demonstrated the epitaxial growth of $CsPbBr_3$ on various substrates[12a–c] which exhibit excellent charge transport properties for optoelectronics applications. While few studies have reported the successful growth of large size single-crystalline $CsPbBr_3$ grains via CVD method and unravel their CVD growth mechanism are highly demanded and urgently needed.

Here we demonstrate for the first-time the CVD growth of $CsPbBr_3$ single-crystalline film with gains having a lateral dimension up to millimeter-scale by properly optimizing the parameters like flow rate, deposition position, and temperature. Obtained $CsPbBr_3$ millimeter single crystal grain shows superior crystallinity without internal strain or defects. The crystal structure, phase purity, and crystallinity are confirmed by X-ray diffraction (XRD) and photoemission characterizations. Moreover, the growth kinetics are further investigated in details with the comparative experiments show the nuclei density and growth rate significantly influence the size, crystallinity, and phase purity of the resulting crystal grains. Finally, we fabricate a lateral PIN diode within one large crystalline grain to demonstrate the emerging electronic properties. Upon illumination, the large crystal device shows high photo-generated voltage of 750 mV and a large photocurrent at zero-bias, suggesting a near-ideal charge collection across a long channel with negligible recombination of carriers. Our demonstration suggests that CVD grown $CsPbBr_3$ crystalline films are promising materials for opto-electronics and high energy detectors application.

2. Results and Discussion

2.1. Material Preparation and Characterization

Figure 1a shows the crystal structure of orthorhombic phase $CsPbBr_3$, which consists of $PbBr_6^{4-}$ octahedrons with Cs^+ cations that occupies the interstitial site to stabilize the crystal structure. Figure 1b illustrates the CVD set-up used in this study. Here we use a two-zone furnace with a quartz tube for growth. One end is connected to Ar as carrier gas and the other end is connected to a vacuum pump. The $CsPbBr_3$ powder is first synthesized by solution method[15] and is placed in the heating zone-I and pre-cleaned glass substrates are placed in the zone-II. For source materials, we have tried both pre-synthesized $CsPbBr_3$ micro-crystal powder and mixtures of precursor powders ($CsBr/PbBr_2$) with different molar ratios (1:1 and 2:1), and found the pre-synthesized $CsPbBr_3$ powder produced thin film with higher purity than that from the mixed precursors. The samples grown with different precursor ratios in a mixture are also studied and shown in Figure S1, Supporting Information. Figure 1c shows the polarized optical microscopy (OM) image for a typical $CsPbBr_3$ crystalline
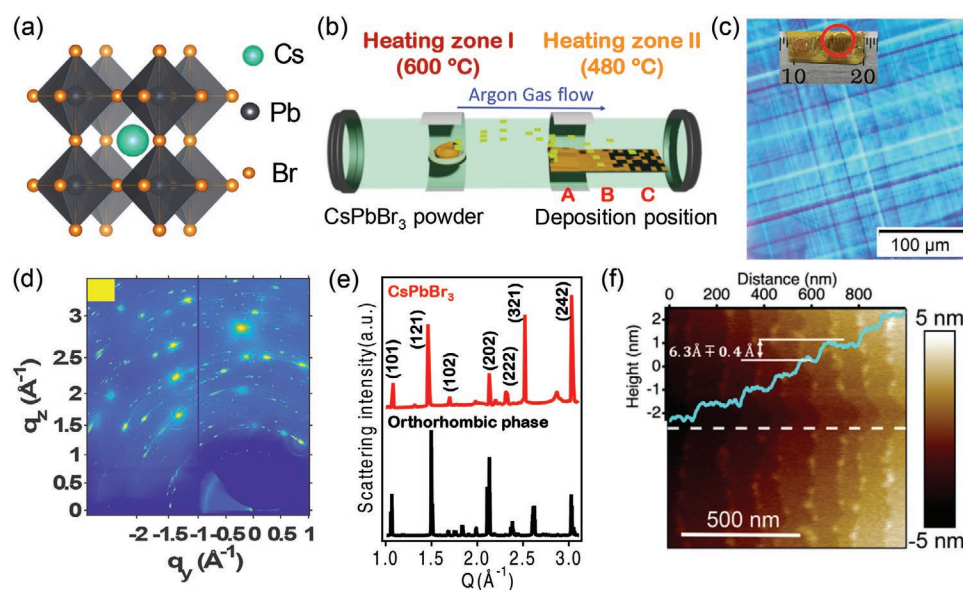

Figure 1. a) Crystal structure of $CsPbBr_3$. b) Schematic illustration of CVD setup: A two-zone furnace, where the precursor is placed at zone-I, and substrate positions (marked as A, B, and C) are placed in zone-II. c) Polarized optical microscopy (OM) image for a single grain. The inset is the photograph of CVD grown $CsPbBr_3$ film with mm-scale grains. d) GIWAXS map of the single crystal $CsPbBr_3$ thin film, and e) the corresponding line-cut extracted from GIWAXS map (red) and simulated X-ray diffraction pattern (black) of orthorhombic phase $CsPbBr_3$. f) AFM image of the surface of the large grain.

**ADVANCED
SCIENCE NEWS**
www.advancedsciencenews.com

**ADVANCED
FUNCTIONAL
MATERIALS**
www.afm-journal.de

grain grown under the optimized CVD growth condition. The OM image exhibits ordered and repeated optical interference fringes, which normally can be observed in high quality single crystal. The inset in Figure 1c is the photo of a CsPbBr$_3$ thin film crystal. From Figure 1c, we notice that the thin film sample has a semi-transparent large crystal grain, the crystal surface is smooth and flat without significant cracks such as protrusions or depressions (multi-polarized angle optical images shows crystal homogeneity in Figure S2, Supporting Information). Moreover, gazing incidence wide angle X-ray scattering (GIWAXS) is further employed to characterize the thin film crystal structure and crystallinity. Note the synchrotron beam spot is small (50 μm width with 0.2 cm footprint) on the sample, and the diffraction pattern is thus obtained from a single crystal thin film domain. As shown in Figure 1d, the GIWAXS map shows discrete dot features which indicate a high degree of crystallinity.[4c,16] The line-cut analysis from the GIWAXS map is compared with the simulated XRD pattern of CsPbBr$_3$, see Figure 1e. In the line-cut pattern of our CVD growth CsPbBr$_3$ thin film, all the peaks can be much indexed with the simulated orthorhombic phase CsPbBr$_3$ diffraction patterns. Moreover, we noticed that the X-ray scattering peaks obtained from the GIWAXS pattern of the CVD grown large crystal sample are sharp compared to previous reports in perovskite thin film[4,17] and nanowire,[18] suggesting a greatly improved crystallinity. The line-cut peaks have full width at the half maximum (FWHM) in the range of 0.0042–0.0126 Å^{-1}, which are much sharper in comparison to the spin coated polycrystalline samples.[19]

To perform a deeper analysis on the crystalline structure of the large grain layer, we employed the atomic force microscopy (AFM) in Figure 1f and scanning electron microscopy (SEM) to probe the micro structure and the composition of the crystalline surface. Interestingly, while the crystal surface looks smooth in macroscopic scale observed by OM and SEM (Figures S2 and S3, Supporting Information), layered structures are present in nano-scale revealed by the AFM images. The height of the steps is estimated to be 6.3 ± 0.4 Å. Similar layered structure was observed in solution grown perovskite single crystals[20] and was attributed to the terminating facet near the surface due to a preferred growth orientation along (101) plane. We think this occurs in our growth process because the crystal prefers to grow along (101) plane of CsPbBr$_3$. As a consequence, larger features could be observed on the surface as a "step-like" feature when the crystal growth terminates. We expect such features could be minimized when the growth rate is carefully controlled. These results suggested that the large CsPbBr$_3$ thin film crystal grains grown by CVD have excellent quality close to a single crystal.

2.2. Crystal Growth Kinetics

To understand the growth kinetics, we identified two most critical growth parameters: 1) the flow rate (in standard cubic centimeter per minute, sccm) of the carrier gas through the quartz tube and 2) distance from the source to the substrate. In order to better analyze the material growth at a specific position, we place three substrates (labeled as A, B, and C) in the heat zoon-II at a distance of 16, 18.5, and 21 cm from the activation source

in heating zone-I, as shown in Figure 1b. At each position, we varied the flow rate from 30 to 120 sccm. Other parameters, such as different ratio of source materials, growth time, growth temperature. and types of substrates (silicon wafer, mica, and nickle oxide (NiO)-glass), and the thin film characterizations (OM images, XRD spectra, and absorption spectra) are also investigated and summarized in Figures S3 and S4, Supporting Information. **Figure 2**a are typical OM images of CsPbBr$_3$ thin film grown under three different flow rates respectively (30, 60, and 120 sccm) at position B. When the flow rate is set to 30 sccm (Figure 2a, multiple crystals with an average grain size of 50 μm in diameter are formed, and the crystalline grains are mostly irregularly shaped that are piled on top of other small grains. This indicates the flow rate of 30 sccm is too slow that allows for high density of nucleation occurring randomly on the substrate. Moreover, the transmission polarized OM images were used to characterize the individual crystal, due to the birefringence of the crystal structures, different colors are expected when multiple crystal axis orientations are present.[21] As shown in Figure 2a, the color of each domain of the 30 sccm samples changes differently, suggesting different crystal orientations and packing are present in each grain. In sharp contrast, once the flow rate increased to 60 and 120 sccm the crystal grains can be grown into much larger sizes (Figure 2b,c). Repeating optical fringes are observed within the crystal grains, the regular fringes suggest highly textured crystalline quality. At flow rate of 120 sccm, the CsPbBr$_3$ thin films have a comparable quality and coverage with the film grown at 60 sccm, but some defects appear on the crystal grain surface (Figure 2c). Besides, upon flow rate increasing, we observed the number of crystal grains decreased in the same substrate area which suggested the flow rate is optimized for nuclei formation and deposition.

There are many parameters that can affect the thin crystal growth mechanism, specially the flow rate and substrate from the activation source location are most important parameters for optimization of the growth process. The process of CVD thin crystal growth follows two steps: I) the transport of active molecules and II) incorporation the molecules into the substrate lattice. In order to further quantitatively examine the crystalline grain growth, we summarized the crystal grain size distribution under different conditions (substrate position and flow rate). Because of the large difference in grain size observed in the samples grown under different conditions (from ≈15 to 3000 μm in diameter), by simply counting the number of grains do not represent the quality of the samples. To evaluate the crystal size distribution, we define a quantity called "percentage of grain area" by:

$$\frac{\text{Area of one grain}}{\text{Area of all samples}} \times 100\% \tag{1}$$

where area of one grain is the area of each grain, and area of all samples is defined by the sum of all the counted grain areas. Figure 2d–f shows the grain size distribution charts, the y-axis is the percentage of grain area, x-axis is the size of crystal grain.

At different growth positions, we found that the grains have a broadened size distribution, and they vary greatly under different flow rate. For position A (Figure 2d), only 60 sccm group has large crystal grains (size over 1000 μm). For position B
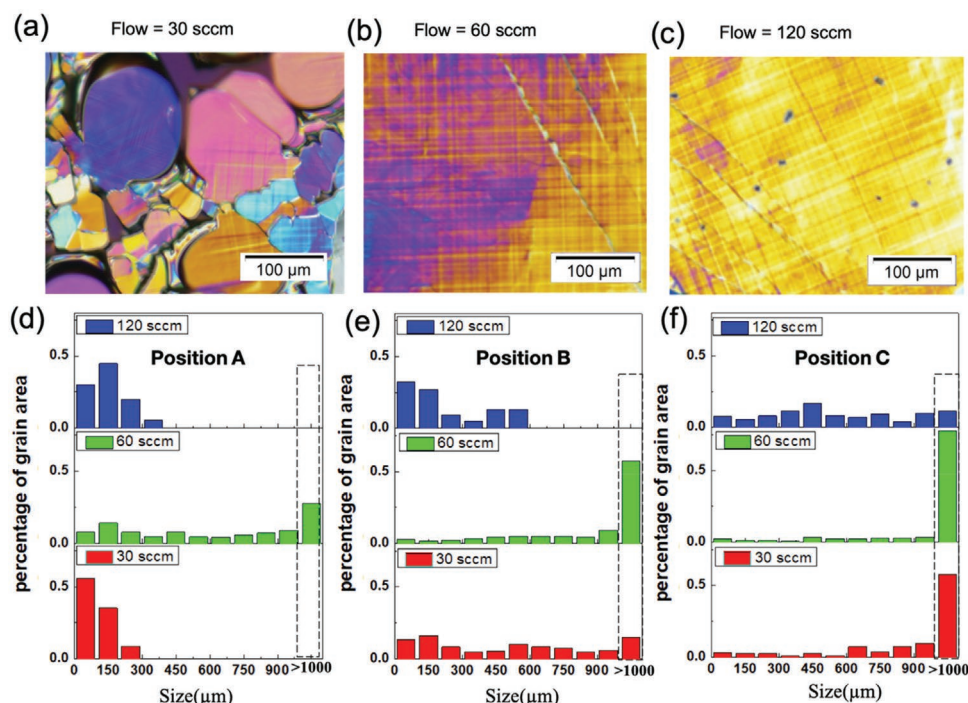
**ADVANCED
SCIENCE NEWS**
www.advancedsciencenews.com

**ADVANCED
FUNCTIONAL
MATERIALS**
www.afm-journal.de

Figure 2. Polarized optical microscopy images of CsPbBr$_3$ crystalline thin films grown at a gas flow rate of a) 30, b) 60, and c) 120 sccm. Crystal grains size distribution at d) position A, e) position B, and f) position C, red green and blue columns represent gas flow at 30, 60, and 120 sccm, respectively.

(Figure 2e), both 30 and 60 sccm group have large crystal grains. While for position C (Figure 2f), large grains can be found in every flow rate groups. Overall, more small grains are observed at position A and B, and larger grains appear in position C as the percentages of large grains area comes to 57.4%. For different flow rates, the largest crystal grain size reaches 2200 µm (at position C) at 30 sccm flow rate group (red column), but most crystal grains show smaller sizes. Within the 60 sccm flow rate group (green column), large crystal grains (over 1000 µm) can be observed at each position and show a broadened size distribution. The largest crystal grain size approaches 3000 µm at position B. For the area percentage, the area of large grains is 27.8% at position A, whereas at position B and position C, the percentages of large grains increased significantly to 57.0% and 77.4% respectively (Figure 2e,f), suggesting the large grains coverage is higher in majority of the substrate area. For the flow rate of 120 sccm (blue column), the small grains cover almost all the areas at position A and B where only few large grains obtained at position C with less percentages of large grains of 11.3% (Figure 2f).

As a short summary, the correlation between the flow rate and substrate location play an essential role for obtaining large thin film crystals. For the position comparison under a fix flow rate, the large crystal grains are more likely to grow when the position is away from the activation source (i.e., B and C location), suggesting that the position B and C at a fix flow rate are more suitable for the growth. In addition, for flow rates comparison under the same substrate location, the large grains prefer to appear more frequently in the 60 sccm groups. This is because the deposition rate is proportional to the flow rate, and the 60 sccm is optimal for crystal growth.

2.3. Material Preparation and Characterization

Apart from the morphology studied in Figure 2, we perform more detailed XRD measurements to characterize the crystallinity and phase purity in **Figure 3** for those CVD growth conditions. Figure 3a shows the normalized XRD patterns for the all CsPbBr$_3$ crystalline thin films synthesized at various CVD growth conditions (substrate position and carrier gas flow rate). Three main diffraction peaks of CsPbBr$_3$ located at $2\theta = 15.3°$, 21.7°, and 30.8°, which are assigned to (101), (121), and (202) lattice planes of orthorhombic phase perovskites at room temperature.[8,10b,c] Interestingly, we observed the dominant peaks (101)/(202) peaks in CVD growth CsPbBr$_3$ crystals in a $\theta/2\theta$ scan which suggest the preferred growth facets parallel to (101) orthogonal plane.[10b] Among the three main peaks, other small peaks can also be the index, which attributed to the orthorhombic phase of CsPbBr$_3$ by comparing with the simulated orthorhombic phase (Figure S5, Supporting Information) and other reports.[22] For instance, the peaks between $2\theta = 22°$ to 29° represent the (102),(112), (220), (131), and (221) planes which are the signature features of orthorhombic phase (Figure 3a). We also observed the Cs$_4$PbBr$_6$ peaks in flow rate = 30 sccm at position A (Figure 3a) which can be matched with reported literatures.[10b] This also suggested that small grains CsPbBr$_3$ crystal has higher chance to co-exist various phases during CVD growth. Besides, the (101) and (202) peaks intensity varies in different growth conditions. Therefore, we summarized the (101)/(202) peak ratio and their corresponding FWHM under different growth conditions to quantify the quality of the CVD grown crystals. In Figure 3d, the (101)/(202) peak ratio are comparably low for all flow rate at position A, and it varies more significantly at position B and C. The 60 sccm flow rate at position
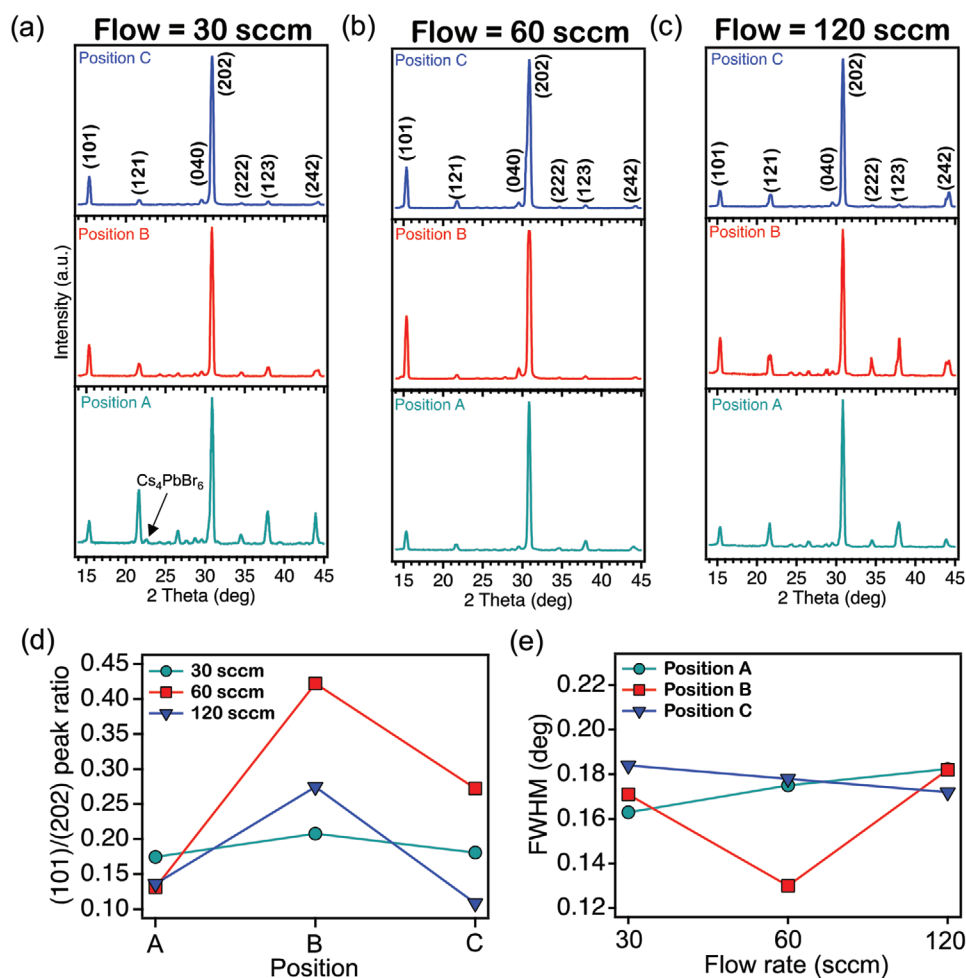
Figure 3. XRD characterization of CVD growth CsPbBr$_3$ thin film at different gas flow rate of a) 30, b) 60, and c)120 sccm, and at different position: A (turquoise), B (red), and C (blue). The d) (101)/(202) peak ratio and e) FWHM analysis for CVD growth condition under various different substrate positions and carrier gas flow rates.

B has the highest peak ratio among the all CVD growth conditions. We further extract the FWHM for the (202) main peak from all growth conditions in Figure 3e. Specifically, the peaks for samples grown under the optimized conditions (60 sccm and position B) have much pronounced peak splitting with relatively narrow FWHM of 0.17° (101) and 0.13° (202), which indicates the better crystallinity and are significantly sharper compared to polycrystalline films fabricated by spin-coating method (FWHM = 0.28° (101) and 0.17°(202)).[23] The higher peak ratio, more pronounced peak splitting, and narrower peak width for sample grown at position-B under 60 sccm rate are indications of high degree of crystallinity, consistent with the grain size analysis in Figure 2.

From the results in Figures 2 and 3, we learn that both optimizing the gas flow rate and finding the ideal growth location from activation source are crucial for obtaining high quality crystalline thin films. Noticeably, these two growth conditions are often coupled. The physical parameters associated with the growth location include material deposition rate and substrate temperature. The deposition rate is also coupled with gas flow rate, that is, a high flow rate results in an optimized growth location farther away from the source. Furthermore, we know that the temperature at different substrate locations can differ by about 20 °C (see in Figure S6, Supporting Information) and

the temperature at position B is about 450 °C in absence of gas flow. To understand the impact of the substrate temperature, we modify the substrate temperature (480, 500, and 520 °C) in heating zone-II. The XRD patterns for those samples are plotted in Figure S7, Supporting Information. As we raised up the deposition temperature from 480 to 520 °C, the orthorhombic phase decreased, which result from the changed growth condition, not contradiction to the phase transition process.[22b,24] The XRD spectrum collected from sample deposition temperature at 480 °C has much stronger diffraction peaks intensity while the XRD spectra collected at elevated substrate temperatures (500 and 520 °C) have higher background and the lower peaks intensity. Therefore, the best signal-to-noise level is achieved in 480 °C deposition condition. This indicates that temperature higher than 480 °C has a reverse effect on the thin film crystallinity, thus lowers the quality of crystalline films.

As a brief summary for the CVD growth process, we have considered the morphology and quality of CsPbBr$_3$ crystal grown under different deposition positions that represent both distance and temperature gradient, as well as the flow rates associated to the deposition kinetics. In order to form crystals, nucleation energy and effective crystallization activation energy must be overcome. In the nucleation process, the flow rate also plays an

important role. When the flow rate is too fast, the nuclei density increases rapidly during the initial nucleation step. If the flow rate is too slow, the nuclei are sparsely distributed, allowing the crystal grains continue grow. Higher nucleation density results in a large number of small grain growths, and the grains are piled up on the top of each other due to fast deposition, resulting in a rough surface. Besides, the crystal growth rate is determined primarily by two factors: 1) the diffusion rate of the vaporized precursor molecule through carrier gas flow and 2) the deposition/growth rate of the crystal determined by deposition/growth position temperature. Fast flow rate carries excessive vaporized source material to deposition position, and high temperature leads to a faster crystallization kinetics, thus both effects contribute to a high crystallization rate, and a suitable high temperature provide a longer diffusion dis-

tance of raw materials for crystallization avoiding stoichiometric imbalance. Thus, in our experiment, the gas flow rate affects the grain size, and the temperature controls the crystal quality. The effects of these two CVD growth parameters are coupled with each other, thus the optimal combination of both the parameters are required for growing large area, high quality crystals.

2.4. Optical Characterization

The optical properties of CVD grown $CsPbBr_3$ thin films are further investigated using photoluminescence (PL) and optical absorption measurements. **Figure 4**a shows the absorption and PL of CVD grown crystalline film and spin coated film.
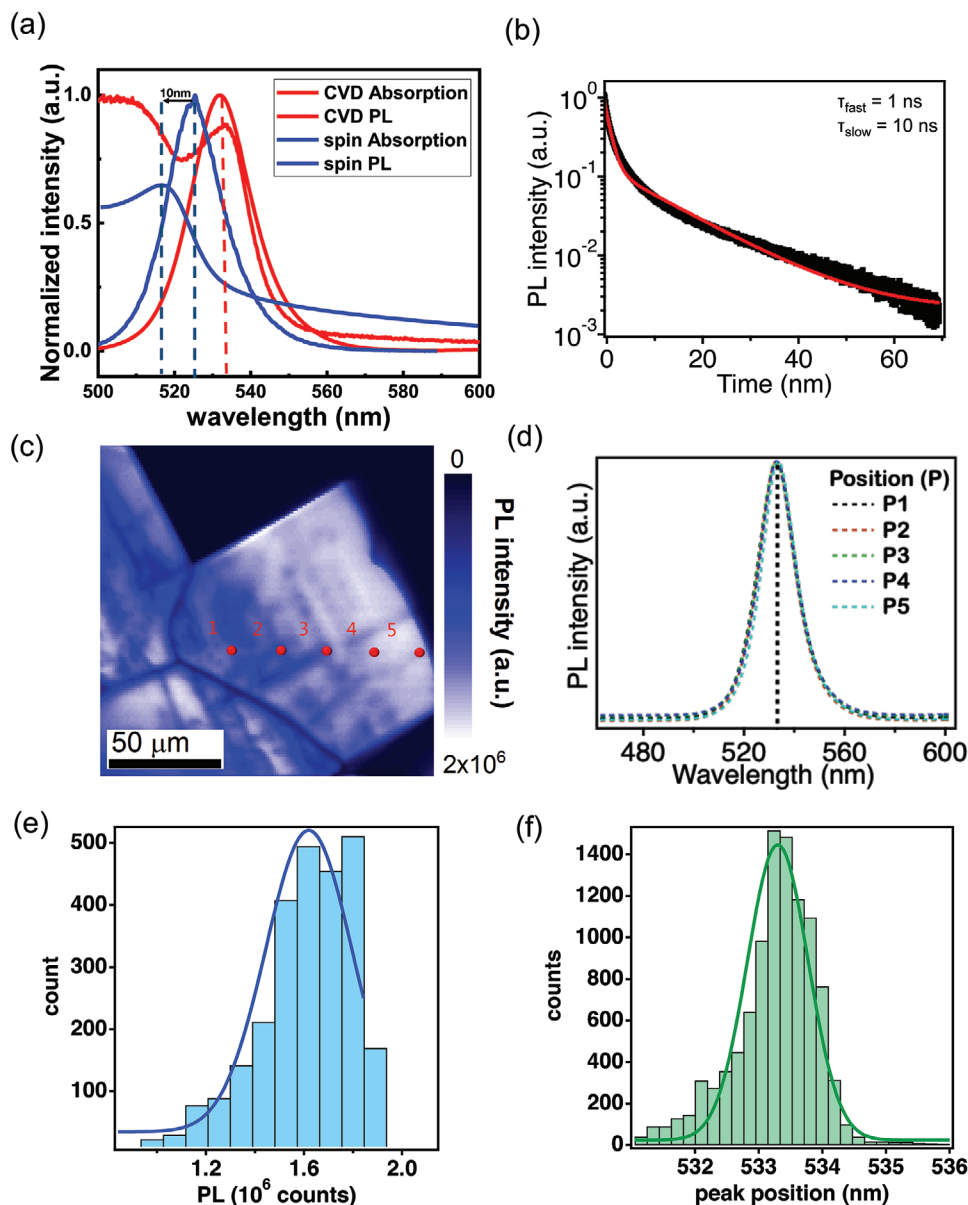

Figure 4. Optical characterization of CVD grown $CsPbBr_3$ films. a) Absorption and PL spectra of CVD growth and spin-coated $CsPbBr_3$ thin film. b) Time-resolve PL decay curve (black) at 532 nm measured with 375 nm excitation. Red line is the bi-exponential fit of the data. c) PL map showing uniform PL intensity (at 532 nm) from crystalline domains larger than 100 micron meters. d) Normalized PL spectra from position 1 to 5 shown in (c). Histogram and the Gaussian fitting (solid lines) of the e) PL peak height and f) peak position extracted from the PL map.

**ADVANCED
SCIENCE NEWS**
www.advancedsciencenews.com

**ADVANCED
FUNCTIONAL
MATERIALS**
www.afm-journal.de

For the CVD grown thin film, we observed a narrow and symmetric PL spectra with a single sharp PL emission peak located at 532 nm (FWHM of 17 nm). In contrast, the spin coated $CsPbBr_3$ thin film show PL centered at 525 nm, which is blue shifted in comparison to the CVD grown sample. Similarly, the absorption spectra for CVD grown film features with an absorption peak at the same wavelength as its PL at around 532 nm, whereas that for the spin coated film is shifted to 518 nm. The blue shift may be attributed to the grain-size effect and thickness effect which is absent in the CVD grown sample.[25] The absorption and PL peak positions overlay well in the CVD grown thin film, suggesting a negligible Stokes shift, which is another indication for large size and uniform crystallite formation in the thin film crystal samples.[26] Besides, absorption spectra of CVD group at various flow rates show good consistency (Figure S8, Supporting Information) which indicates the CVD method has better material growth control with consistent quality. We also performed the time-resolved PL characterization (Figure 4b) where the time-resolved PL trace fits well to a bi-exponential decay model with the fast component (τ_{fast}) and slow component (τ_{slow}). The τ_{fast} is attributed to a trap assisted recombination of carriers near the surface while the τ_{slow} is attributed to a carrier recombination in the bulk. We extract a fast and a slow carrier lifetime component of 1 and 10 ns, respectively which agrees well with other reported literatures.[10b,27] In order to probe the emission uniformity of CVD grown thin film crystal, we further spatially PL mapped a typical CVD grown $CsPbBr_3$ crystal (Figure 4c). From the obtained PL mapping image, it is clear that the crystalline domains are larger than 100 microns with well-resolved sharp edges. A PL emission height variation is observed from the outer grain to the inner boundary, which is likely attributed to the thickness increase near the outer edge. The normalized PL spectra taken from five different positions on the crystalline domains (red points in the Figure 4c) can overlay perfectly (Figure 4d), suggesting highly uniform optical properties across the large area CVD growth $CsPbBr_3$ crystal. This is reflected in the histogram plot that describes the distribution of the PL height and peak position in Figure 4e. The PL peak position is centered around 533 nm with negligible variation of 1–2 nm across the full area. In sharp contrast, the small grain sample (Figure S9, Supporting Information) shows significant PL variations in both PL intensity and PL peak positions.

2.5. Electrical Characterization

In order to demonstrate the opto-electronic performance of CVD grown $CsPbBr_3$ thin film with large crystalline grains, a lateral device is fabricated in a single large grain (dubbed as large grain device), where asymmetric Au and Ag contacts are deposited. A 175 µm gap is used between two circular contacts as shown in **Figure 5**a (for details device preparation, see Experimental Section). As a comparison, device with the same structure is fabricated on a CVD grown film with small grains (dubbed as small grain device). Voltage sweeps from −3 to +3 V are done on the device in dark and under 1-sun illumination to compare the charge collection characteristics. Figure 5b and

Figure S10, Supporting Information show the current–voltage (J–V) curve under 1-sun illumination on the device producing a diode behavior. The lateral devices demonstrate diode characteristics (rectifying behavior) due to the asymmetric work functions of the electrodes illustrated in Figure 5d. Zoom-in view of the circled area in Figure 5b is represented in Figure 5c. Inset shows photographs of the large and small grain devices studied here. In both devices, a photo-generated open circuit voltage (V_{OC}) and short circuit current (J_{SC}) are observed in the J–V curves. A large V_{OC} of 750 mV and J_{SC} of 1.567 µA cm^{-2} are generated for the large grain device. In sharp contrast, the small grain device only exhibits low V_{OC} of 550 mV with J_{SC} of 0.464 µA cm^{-2}. To compare the dark and photocurrent, in Figure 5e,f, we plot the dark and light J–V curves for both large grain and small grain devices in log-linear scale (the dark currents are plotted in Figure S11, Supporting Information). In addition, we calculated the switch ratio (SR) of the two devices defined by: SR = $[(I_{light}-I_{dark})/I_{dark}]$, where I_{light} is photocurrent and I_{dark} is dark current. Interestingly, the dark current for the large grain device is lower than the small grain device, whereas the photocurrent is much higher for the large grain device. The low dark current observed in the large grain device is due to the suppressed dark recombination from traps, which thus make the difference ($J_{light}-J_{dark}$) significantly larger than small grain device. The peak SR is found to be 420 for the large grain device at 0.2 V, whereas the peak SR is 30 near 0.2 V.

Moreover, to understand the recombination mechanisms of photogenerated carriers during device operation, we measure the J_{SC} and V_{OC} as a function of light intensity in log scale for both devices (Figure 5g). Light intensity dependence of J_{SC} in log–log scale is conducted to understand the effect of the crystal size on the photo-current collection efficiency where linear response for J_{SC} versus illumination light intensity indicates an ideal charge collection ability. As presented in Figure 5g, the large grain device shows an ideal linear dependent relation, whereas the small grain device has a sub-linear dependence at low illumination powers. Note that the channel length is 175 µm in the later device and the electrical field is dropping rapidly near the electrode,[28] subsequently the photo-generated carrier collection at short circuit mostly rely on carrier diffusion. Therefore, a near linear dependence in J_{SC} as a function of illumination power suggests that trap assisted recombination is negligible in the single large grain device. The semi-log plot in Figure 5h shows that the V_{OC} of the large grain device also increases with light intensity, as the linear fit has a slope of 40 meV, which corresponds to 1.6 k_BT/q (k_B is the Boltzmann constant, T is the temperature, and q is elementary charge). Figure 5i shows a schematic diagram of the energy barriers that we believe contribute to the charge scattering. Across the grain boundaries, the energy barriers can appear due to broken chemical bonds and lattice mismatch. For small grain device, the carriers have high chance to be trapped near the grain boundaries when charge carriers have to travel though several grain boundaries to reach contacts. Therefore, it will form energy barriers, which is detrimental for the charge collection at the contacts and resulting in a lower V_{OC} compared to large grain device, there are less grain boundaries which leads to a much-reduced charge trapping problem with obtained higher V_{OC}.
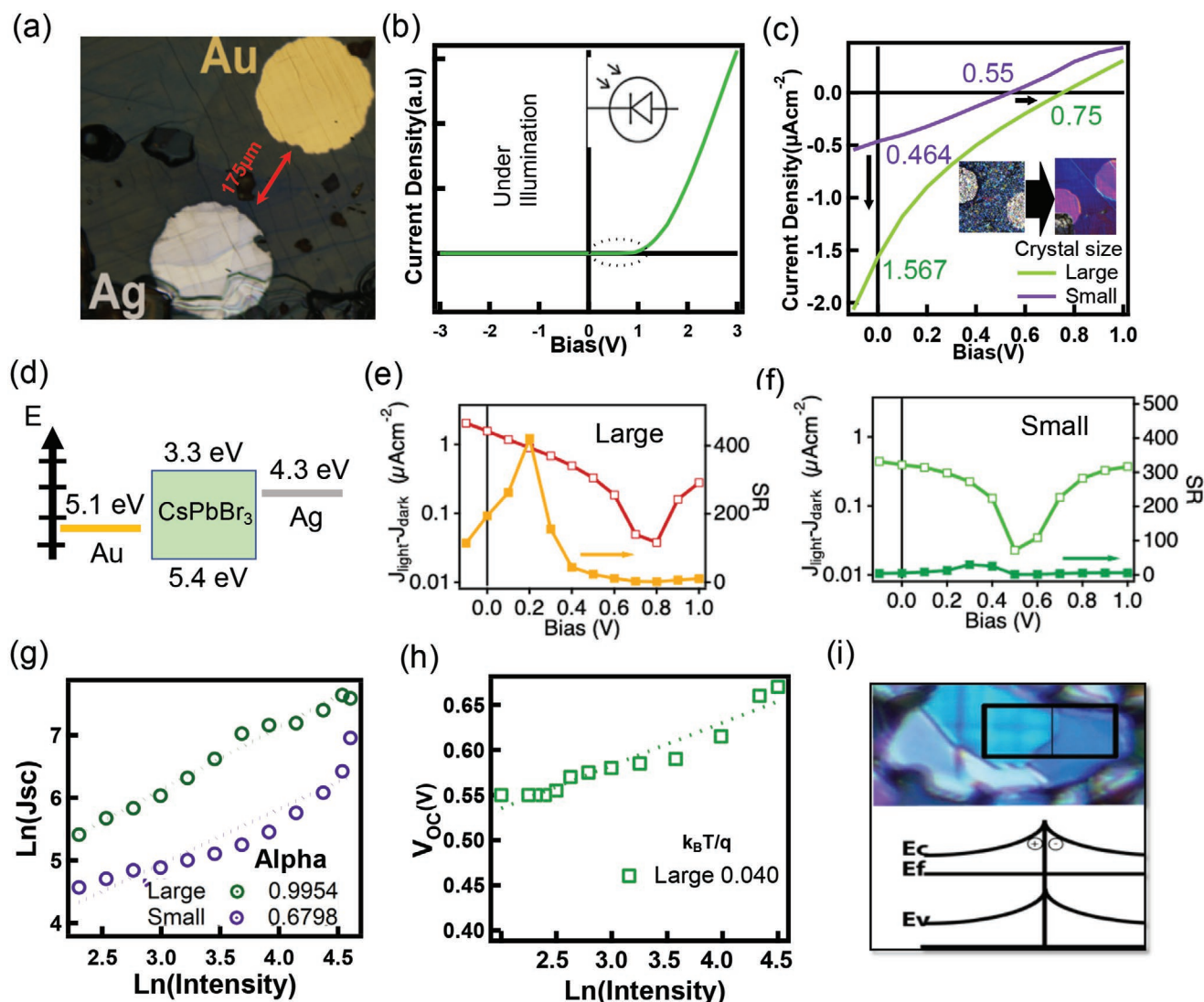
Figure 5. Electrical characterization. a) Lateral device on a single $CsPbBr_3$ crystal grain. b) The J–V curve of the lateral device under 1 sun illumination. c) Zoomed view of circled area in (b). d) Energy alignment diagram for the lateral device. e,f) The difference of dark and photocurrent and their SR as a function of bias. g) Light intensity dependent short circuit current J_{SC} and h) light intensity dependence on open circuit voltage V_{OC} of devices fabricated on one large crystal grain. i) Schematic diagram of energy-band shows the energy barrier appearing across the grain boundaries.

3. Conclusion

In summary, we report a simple one step CVD method to synthesize $CsPbBr_3$ films with millimeter sized crystalline grains featuring high purity and crystallinity. The largest crystal grain observed has a lateral dimension over 3.1 mm. The polarized OM images, XRD analysis, and optical and electrical measurements confirmed the high quality of CVD growth crystalline samples. Through detailed analysis of experimental results, we conclude that the growth rate plays a decisive role in the crystalline quality. Experimental parameters such as gas flow rate and deposition position from the source govern the growth rate that subsequently lead to large grain growth.

In the literature, pioneer works have reported various structures that can be grown by CVD method. For instance, micron sized crystallites can be grown epitaxially on single crystal substrates;[12a,14,25] nanowires as well as heterostructures are also demonstrated for high performance photo-detectors.[12c,29] In order to achieve large scale growth with well controlled nano/micron structures, the growth conditions worth in-depth investigations. In our study, we found to reach large crystal grain growth, the key physical parameter to control is the crystal growth rate. After carefully tuning the growth parameters, we found that the growth rate is determined by the gas flow rate and the deposition location, that is, source to substrate distance, in the CVD process. We believe our growth parameters and mechanisms can be employed to scale up the nano- and micron- structures growth described in the literatures.

4. Experimental Section

Materials: Caesium bromide (CsBr, 99.5%) and lead bromide (PbBr₂, 99.0%), hydrobromic acid (HBr, 48 wt% in water), DMSO, and methanol

(MeOH, 100%) were purchase from Sigma Aldrich and used as received without further purification.

Synthesis of CsPbBr₃ Powder: For the CsPbBr₃ powder synthesis, the PbBr₂ powder (3.65 g, 10 mmol) was first dissolved in a concentrated HBr (15 mL), the PbBr₂ powder was completely dissolved and became transparent solution with pale yellow color. Meanwhile, the CsBr powder (2.13 g, 10 mmol) was dissolved in deionized water (5 mL) to obtain CsBr aqueous solution. The CsBr solution was added drop wisely to the PbBr₂/HBr solution under constant stirring. The orange precipitates were the final product of the CsPbBr₃ powder. The mixture solution was stirred for another 10 min, followed by being filtered to extract the orange precipitates, the precipitates were washed by methanol after extraction. The collected orange powder was then dried by vacuum at room-temperature for two hours.

Fabrication of CsPbBr₃ Film by Spin Coating Method: First, PbBr₂ (10 mmol) and CsBr (10 mmol) were dissolved in DMSO (10 mL) and stirred for one hour with heating at 120 °C. Then use 200 µL solution to fabricate on pre-cleaned glass substrate by spin coating with 1500 rpm for 30 s. The spin coated thin film was moved to hot plate and heated at 150 °C for 10 min for removing excess solvent.

CVD Growth CsPbBr₃ Thin Film: In a typical CVD growth process, a carrier gas (argon) was passed through the sealed quartz tube which was pumped under a pressure of about 3.0 milli-Torr. To control the quartz tube temperature, heating zone I was kept at 600 °C which corresponds to the melting point temperature of CsPbBr₃.[1c] The pre-synthesized CsPbBr₃ powder was used for activation source. The substrates of glass, wafer, mica, and NiO/glass were rinsed with MeOH and cleaned by ozone plasma for removing the surface impurities. The substrates were placed in the heating Zone II and the tube was pumped and purged with carrier gas for several times. The carrier gas flow rates (sccm) and zone-II temperatures were optimized for the large-area with best quality crystals. The optimized flow rate was 60 sccm with deposition process of 60 min after heating zones I reached the desire temperature. After fabrication process finished, the CVD set-up was naturally cooled to room temperature.

For precursor ratio optimization the mixture of precursor powders (CsBr and PbBr₂) with different molar ratios (1:1 and 2:1) were used as the source materials and placed in the heating zone-I under fix CVD growth conditions (gas flow rate 60 sccm, heating zone-I 600 °C, and growth time 60 mins).

For growth time optimization group, only growth times of 30 and 60 min were employed, other details were fixed as same condition (gas flow rate: 60 sccm, heating zone-I: 600 °C). Figure S2c,d, Supporting Information. For deposition temperature comparison group, the heating zone II was set at 480, 500, and 520 °C for comparison.

Crystal Grain Size Distribution Analysis Samples Details: All the obtained samples were chosen from 360 substrates with total numbers of 6800 crystals.

Photoluminescence Measurement Details: PL spectroscopy and map were obtained using a custom-built setup consisting of a 405 nm laser (Thor labs) and a 50× objective lens with a numerical aperture of 0.50. The laser spot size was roughly between 1 and 2 microns. Neutral density filters were used to reduce the laser intensity. PL spectra were measured by a spectrograph (Princeton instruments, Pro EM 1024). The samples were mounted on a piezoelectric stage (Mad City Labs Inc., Nanodrive) and scanned with a step size of 1 micron for PL mapping. Time resolved PL measurements were performed using a 375 nm pulsed laser (PDL 800-B) with a pulse width of 40 ps and average power of 0.5 mW at a repetition frequency of 5 MHz. An avalanche photo-diode (MPD-SPAD) and a time correlated single photon counting module (PicoHarp 300) were used to measure the photon counts at 530 nm to obtain time resolved PL and PL map. The measurements were done at room temperature under ambient conditions.

Device Fabrication and Characterizations: Following method was used to fabricate the two terminal lateral solar cells using small and large sized crystals of CsPbBr₃. As shown in the Figure 5a shadow mask with 100 µm circular opening was used to make the top contacts on the crystals. The large sized crystal was selected from CVD grown crystals on the glass slides. A shadow mask with 100 µm circular opening was used to make the top contacts on the crystals. One contact material (Au-100 nm) first deposited using e-beam deposition, and manually shifting the mask by ≈150 µm where both the contacts lie on the same grain. Second layer of contact material (Ag-100 nm) was deposited on the crystals using thermal deposition. For small grains device, the process was the same as large grain device. The devices were then transfer to cryostat chamber and pump the chamber to high vacuum (1e-7 torr) level. The device in cryostat chamber was connected by Pogo pins with external circuit connection. Between each scan, the new scans were kept in dark with no bias before the next scan.

Supporting Information

Supporting Information is available from the Wiley Online Library or from the author.

Conflict of Interest

The authors declare no conflict of interest.

Data Availability Statement

The data that support the findings of this study are available from the corresponding author upon reasonable request.

[1] a) S. D. Stranks, G. E. Eperon, G. Grancini, C. Menelaou, M. J. P. Alcocer, T. Leijtens, L. M. Herz, A. Petrozza, H. J. Snaith, *Science* **2013**, *342*, 341; b) T. Chen, W.-L. Chen, B. J. Foley, J. Lee, J. P. C. Ruff, J. Y. P. Ko, C. M. Brown, L. W. Harriger, D. Zhang, C. Park, M. Yoon, Y.-M. Chang, J. J. Choi, S.-H. Lee, *Proc. Natl. Acad. Sci. U. S. A.* **2017**, *114*, 7519; c) J. Jiang, X. Sun, X. Chen, B. Wang, Z. Chen, Y. Hu, Y. Guo, L. Zhang, Y. Ma, L. Gao, F. Zheng, L. Jin,

M. Chen, Z. Ma, Y. Zhou, N. P. Padture, K. Beach, H. Terrones, Y. Shi, D. Gall, T.-M. Lu, E. Wertz, J. Feng, J. Shi, *Nat. Commun.* **2019**, *10*, 4145; d) J. Tong, Z. Song, D. H. Kim, X. Chen, C. Chen, A. F. Palmstrom, P. F. Ndione, M. O. Reese, S. P. Dunfield, O. G. Reid, J. Liu, F. Zhang, S. P. Harvey, Z. Li, S. T. Christensen, G. Teeter, D. Zhao, M. M. Al-Jassim, M. F. A. M. van Hest, M. C. Beard, S. E. Shaheen, J. J. Berry, Y. Yan, K. Zhu, *Science* **2019**, *364*, 475.

[2] a) J. Lim, M. T. Hörantner, N. Sakai, J. M. Ball, S. Mahesh, N. K. Noel, Y.-H. Lin, J. B. Patel, D. P. McMeekin, M. B. Johnston, B. Wenger, H. J. Snaith, *Energy Environ. Sci.* **2019**, *12*, 169; b) C. Wehrenfennig, G. E. Eperon, M. B. Johnston, H. J. Snaith, L. M. Herz, *Adv. Mater.* **2014**, *26*, 1584.

[3] a) F. Wang, S. Bai, W. Tress, A. Hagfeldt, F. Gao, *npj Flexible Electron.* **2018**, *2*, 22; b) W.-J. Yin, T. Shi, Y. Yan, *Appl. Phys. Lett.* **2014**, *104*, 063903.

[4] a) M. Liu, M. B. Johnston, H. J. Snaith, *Nature* **2013**, *501*, 395; b) M. Saliba, T. Matsui, J.-Y. Seo, K. Domanski, J.-P. Correa-Baena, M. K. Nazeeruddin, S. M. Zakeeruddin, W. Tress, A. Abate, A. Hagfeldt, M. Grätzel, *Energy Environ. Sci.* **2016**, *9*, 1989; c) H. Tsai, W. Nie, J.-C. Blancon, C. C. Stoumpos, R. Asadpour, B. Harutyunyan, A. J. Neukirch, R. Verduzco, J. J. Crochet, S. Tretiak, L. Pedesseau, J. Even, M. A. Alam, G. Gupta, J. Lou, P. M. Ajayan, M. J. Bedzyk, M. G. Kanatzidis, A. D. Mohite, *Nature* **2016**, *536*, 312; d) M. Yang, Z. Li, M. O. Reese, O. G. Reid, D. H. Kim, S. Siol, T. R. Klein, Y. Yan, J. J. Berry, M. F. A. M. van Hest, K. Zhu, *Nat. Energy* **2017**, *2*, 17038; e) B. Zhao, L. C. Lee, L. Yang, A. J. Pearson, H. Lu, X.-J. She, L. Cui, K. H. L. Zhang, R. L. Z. Hoye, A. Karani, P. Xu, A. Sadhanala, N. C. Greenham, R. H. Friend, J. L. MacManus-Driscoll, D. Di, *ACS Appl. Mater. Interfaces* **2018**, *10*, 41849; f) Y. Lei, Y. Chen, R. Zhang, Y. Li, Q. Yan, S. Lee, Y. Yu, H. Tsai, W. Choi, K. Wang, Y. Luo, Y. Gu, X. Zheng, C. Wang, C. Wang, H. Hu, Y. Li, B. Qi, M. Lin, Z. Zhang, S. A. Dayeh, M. Pharr, D. P. Fenning, Y.-H. Lo, J. Luo, K. Yang, J. Yoo, W. Nie, S. Xu, *Nature* **2020**, *583*, 790; g) J. Li, H. Wang, X. Y. Chin, H. A. Dewi, K. Vergeer, T. W. Goh, J. W. M. Lim, J. H. Lew, K. P. Loh, C. Soci, T. C. Sum, H. J. Bolink, N. Mathews, S. Mhaisalkar, A. Bruno, *Joule* **2020**, *4*, 1035; h) F. Liu, M. Yoho, H. Tsai, K. Fernando, J. Tisdale, S. Shrestha, J. K. Baldwin, A. D. Mohite, S. Tretiak, D. T. Vo, W. Nie, *Mater. Today* **2020**, *37*, 27; i) S. Sánchez, J. Jerónimo-Rendon, M. Saliba, A. Hagfeldt, *Mater. Today* **2020**, *35*, 9; j) H. Tsai, F. Liu, S. Shrestha, K. Fernando, S. Tretiak, B. Scott, D. T. Vo, J. Strzalka, W. Nie, *Sci. Adv.* **2020**, *6*, eaay0815; k) C.-Y. Chang, H.-H. Huang, H. Tsai, S.-L. Lin, P.-H. Liu, W. Chen, F.-C. Hsu, W. Nie, Y.-F. Chen, L. Wang, *Adv. Sci.* **2021**, *8*, 2002718.

[5] a) L. Protesescu, S. Yakunin, M. I. Bodnarchuk, F. Krieg, R. Caputo, C. H. Hendon, R. X. Yang, A. Walsh, M. V. Kovalenko, *Nano Lett.* **2015**, *15*, 3692; b) J. Xu, W. Huang, P. Li, D. R. Onken, C. Dun, Y. Guo, K. B. Ucer, C. Lu, H. Wang, S. M. Geyer, R. T. Williams, D. L. Carroll, *Adv. Mater.* **2017**, *29*, 1703703; c) L. Zhang, X. Yang, Q. Jiang, P. Wang, Z. Yin, X. Zhang, H. Tan, Y. Yang, M. Wei, B. R. Sutherland, E. H. Sargent, J. You, *Nat. Commun.* **2017**, *8*, 15640; d) H. Wang, X. Zhang, Q. Wu, F. Cao, D. Yang, Y. Shang, Z. Ning, W. Zhang, W. Zheng, Y. Yan, S. V. Kershaw, L. Zhang, A. L. Rogach, X. Yang, *Nat. Commun.* **2019**, *10*, 665.

[6] a) D. N. Dirin, I. Cherniukh, S. Yakunin, Y. Shynkarenko, M. V. Kovalenko, *Chem. Mater.* **2016**, *28*, 8470; b) M. I. Saidaminov, M. A. Haque, J. Almutlaq, S. Sarmah, X.-H. Miao, R. Begum, A. A. Zhumekenov, I. Dursun, N. Cho, B. Murali, O. F. Mohammed, T. Wu, O. M. Bakr, *Adv. Opt. Mater.* **2017**, *5*, 1600704; c) Q. Xu, X. Wang, H. Zhang, W. Shao, J. Nie, Y. Guo, J. Wang, X. Ouyang, *ACS Appl. Electron. Mater.* **2020**, *2*, 879; d) Y. He, M. Petryk, Z. Liu, D. G. Chica, I. Hadar, C. Leak, W. Ke, I. Spanopoulos, W. Lin, D. Y. Chung, B. W. Wessels, Z. He, M. G. Kanatzidis, *Nat. Photonics* **2021**, *15*, 36.

[7] a) G. Jiang, C. Guhrenz, A. Kirch, L. Sonntag, C. Bauer, X. Fan, J. Wang, S. Reineke, N. Gaponik, A. Eychmüller, *ACS Nano* **2019**, *13*, 10386; b) L. Yang, T. Wang, Q. Min, B. Liu, Z. Liu, X. Fan, J. Qiu, X. Xu, J. Yu, X. Yu, *ACS Omega* **2019**, *4*, 6084; c) P. Song, B. Qiao, D. Song, J. Cao, Z. Shen, G. Zhang, Z. Xu, S. Zhao, S. Wageh, A. Al-Ghamdi, *J. Mater. Sci.* **2020**, *55*, 9739.

[8] C. C. Stoumpos, C. D. Malliakas, J. A. Peters, Z. Liu, M. Sebastian, J. Im, T. C. Chasapis, A. C. Wibowo, D. Y. Chung, A. J. Freeman, B. W. Wessels, M. G. Kanatzidis, *Cryst. Growth Des.* **2013**, *13*, 2722.

[9] a) D. Zhang, S. W. Eaton, Y. Yu, L. Dou, P. Yang, *J. Am. Chem. Soc.* **2015**, *137*, 9230; b) D. Zhang, Y. Yu, Y. Bekenstein, A. B. Wong, A. P. Alivisatos, P. Yang, *J. Am. Chem. Soc.* **2016**, *138*, 13155; c) M. V. Kovalenko, L. Protesescu, M. I. Bodnarchuk, *Science* **2017**, *358*, 745.

[10] a) S. W. Eaton, M. Lai, N. A. Gibson, A. B. Wong, L. Dou, J. Ma, L.-W. Wang, S. R. Leone, P. Yang, *Proc. Natl. Acad. Sci. U. S. A.* **2016**, *113*, 1993; b) Y. Rakita, N. Kedem, S. Gupta, A. Sadhanala, V. Kalchenko, M. L. Böhm, M. Kulbak, R. H. Friend, D. Cahen, G. Hodes, *Cryst. Growth Des.* **2016**, *16*, 5717; c) H. Zhang, X. Liu, J. Dong, H. Yu, C. Zhou, B. Zhang, Y. Xu, W. Jie, *Cryst. Growth Des.* **2017**, *17*, 6426.

[11] a) N. Yantara, S. Bhaumik, F. Yan, D. Sabba, H. A. Dewi, N. Mathews, P. P. Boix, H. V. Demir, S. Mhaisalkar, *J. Phys. Chem. Lett.* **2015**, *6*, 4360; b) X. Zhang, B. Xu, J. Zhang, Y. Gao, Y. Zheng, K. Wang, X. W. Sun, *Adv. Funct. Mater.* **2016**, *26*, 4595; c) I. Dursun, M. De Bastiani, B. Turedi, B. Alamer, A. Shkurenko, J. Yin, A. M. El-Zohry, I. Gereige, A. AlSaggaf, O. F. Mohammed, M. Eddaoudi, O. M. Bakr, *ChemSusChem* **2017**, *10*, 3746.

[12] a) J. Chen, D. J. Morrow, Y. Fu, W. Zheng, Y. Zhao, L. Dang, M. J. Stolt, D. D. Kohler, X. Wang, K. J. Czech, M. P. Hautzinger, S. Shen, L. Guo, A. Pan, J. C. Wright, S. Jin, *J. Am. Chem. Soc.* **2017**, *139*, 13525; b) Y. Wang, X. Sun, Z. Chen, Y.-Y. Sun, S. Zhang, T.-M. Lu, E. Wertz, J. Shi, *Adv. Mater.* **2017**, *29*, 1702643; c) L. Zhao, Y. Gao, M. Su, Q. Shang, Z. Liu, Q. Li, Q. Wei, M. Li, L. Fu, Y. Zhong, J. Shi, J. Chen, Y. Zhao, X. Qiu, X. Liu, N. Tang, G. Xing, X. Wang, B. Shen, Q. Zhang, *ACS Nano* **2019**, *13*, 10085; d) Y. Wang, Z. Wan, Q. Qian, Y. Liu, Z. Kang, Z. Fan, P. Wang, Y. Wang, C. Li, C. Jia, Z. Lin, J. Guo, I. Shakir, M. Goorsky, X. Duan, Y. Zhang, Y. Huang, X. Duan, *Nat. Nanotechnol.* **2020**, *15*, 768; e) Y. Zhong, K. Liao, W. Du, J. Zhu, Q. Shang, F. Zhou, X. Wu, X. Sui, J. Shi, S. Yue, Q. Wang, Y. Zhang, Q. Zhang, X. Hu, X. Liu, *ACS Nano* **2020**, *14*, 15605.

[13] S. Lan, W. Li, S. Wang, J. Li, J. Wang, H. Wang, H. Luo, D. Li, *Adv. Opt. Mater.* **2019**, *7*, 1801336.

[14] X. Mo, X. Li, G. Dai, P. He, J. Sun, H. Huang, J. Yang, *Nanoscale* **2019**, *11*, 21386.

[15] C.-Y. Huang, C.-C. Wu, C.-L. Wu, C.-W. Lin, *ACS Omega* **2019**, *4*, 8081.

[16] a) A. Z. Chen, M. Shiu, J. H. Ma, M. R. Alpert, D. Zhang, B. J. Foley, D.-M. Smilgies, S.-H. Lee, J. J. Choi, *Nat. Commun.* **2018**, *9*, 1336; b) H. Tsai, R. Asadpour, J.-C. Blancon, C. C. Stoumpos, J. Even, P. M. Ajayan, M. G. Kanatzidis, M. A. Alam, A. D. Mohite, W. Nie, *Nat. Commun.* **2018**, *9*, 2130; c) H. Tsai, W. Nie, J.-C. Blancon, C. C. Stoumpos, C. M. M. Soe, J. Yoo, J. Crochet, S. Tretiak, J. Even, A. Sadhanala, G. Azzellino, R. Brenes, P. M. Ajayan, V. Bulović, S. D. Stranks, R. H. Friend, M. G. Kanatzidis, A. D. Mohite, *Adv. Mater.* **2018**, *30*, 1704217; d) F. Wang, X. Jiang, H. Chen, Y. Shang, H. Liu, J. Wei, W. Zhou, H. He, W. Liu, Z. Ning, *Joule* **2018**, *2*, 2732; e) H. Tsai, C. Liu, E. Kinigstein, M. Li, S. Tretiak, M. Cotlet, X. Ma, X. Zhang, W. Nie, *Adv. Sci.* **2020**, *7*, 1903202.

[17] L. Lee, J. Baek, K. S. Park, Y.-E. Lee, N. K. Shrestha, M. M. Sung, *Nat. Commun.* **2017**, *8*, 15882.

[18] J. Feng, C. Gong, H. Gao, W. Wen, Y. Gong, X. Jiang, B. Zhang, Y. Wu, Y. Wu, H. Fu, L. Jiang, X. Zhang, *Nat. Electron.* **2018**, *1*, 404.

[19] a) M. Abdi-Jalebi, Z. Andaji-Garmaroudi, S. Cacovich, C. Stavrakas, B. Philippe, J. M. Richter, M. Alsari, E. P. Booker, E. M. Hutter, A. J. Pearson, S. Lilliu, T. J. Savenije, H. Rensmo, G. Divitini, C. Ducati, R. H. Friend, S. D. Stranks, *Nature* **2018**, *555*, 497; b) W. Nie, H. Tsai, J.-C. Blancon, F. Liu, C. C. Stoumpos, B. Traore, M. Kepenekian, O. Durand, C. Katan, S. Tretiak, J. Crochet, P. M. Ajayan, M. Kanatzidis, J. Even, A. D. Mohite, *Adv. Mater.* **2018**, *30*, 1703879; c) H. Tsai, R. Asadpour, J.-C. Blancon, C. C. Stoumpos, O. Durand, J. W. Strzalka, B. Chen, R. Verduzco, P. M. Ajayan, S. Tretiak, J. Even, M. A. Alam, M. G. Kanatzidis, W. Nie, A. D. Mohite, *Science* **2018**, *360*, 67; d) L. Gao, L. N. Quan, F. P. García de Arquer, Y. Zhao, R. Munir, A. Proppe, R. Quintero-Bermudez, C. Zou, Z. Yang, M. I. Saidaminov, O. Voznyy, S. Kinge, Z. Lu, S. O. Kelley, A. Amassian, J. Tang, E. H. Sargent, *Nat. Photonics* **2020**, *14*, 227.

[20] J. Ding, Y. Zhao, S. Du, Y. Sun, H. Cui, X. Zhan, X. Cheng, L. Jing, *J. Mater. Sci.* **2017**, *52*, 7907.

[21] a) W. Kaminsky, K. Claborn, B. Kahr, *Chem. Soc. Rev.* **2004**, *33*, 514; b) I. W. Hamley, V. Castelletto, R. V. Castillo, A. J. Müller, C. M. Martin, E. Pollet, P. Dubois, *Macromolecules* **2005**, *38*, 463.

[22] a) C. Tian, F. Wang, Y. Wang, Z. Yang, X. Chen, J. Mei, H. Liu, D. Zhao, *ACS Appl. Mater. Interfaces* **2019**, *11*, 15804; b) C. A. López, C. Abia, M. C. Alvarez-Galván, B.-K. Hong, M. V. Martínez-Huerta, F. Serrano-Sánchez, F. Carrascoso, A. Castellanos-Gómez, M. T. Fernández-Díaz, J. A. Alonso, *ACS Omega* **2020**, *5*, 5931.

[23] a) Y. Huang, L. Zhang, J. Wang, B. Zhang, L. Xin, S. Niu, Y. Zhao, M. Xu, X. Chu, D. Zhang, C. Qu, F. Zhao, *Opt. Lett.* **2019**, *44*, 1908; b) C. Tenailleau, S. Aharon, B.-E. Cohen, L. Etgar, *Nanoscale Adv.* **2019**, *1*, 147.

[24] Y. Wang, F. Yang, X. Li, F. Ru, P. Liu, L. Wang, W. Ji, J. Xia, X. Meng, *Adv. Funct. Mater.* **2019**, *29*, 1904913.

[25] Y. Gao, L. Zhao, Q. Shang, Y. Zhong, Z. Liu, J. Chen, Z. Zhang, J. Shi, W. Du, Y. Zhang, S. Chen, P. Gao, X. Liu, X. Wang, Q. Zhang, *Adv. Mater.* **2018**, *30*, 1801805.

[26] M. C. Brennan, A. Forde, M. Zhukovskyi, A. J. Baublis, Y. V. Morozov, S. Zhang, Z. Zhang, D. S. Kilin, M. Kuno, *J. Phys. Chem. Lett.* **2020**, *11*, 4937.

[27] X. Hu, X. Wang, P. Fan, Y. Li, X. Zhang, Q. Liu, W. Zheng, G. Xu, X. Wang, X. Zhu, A. Pan, *Nano Lett.* **2018**, *18*, 3024.

[28] S. Shrestha, H. Tsai, M. Yoho, D. Ghosh, F. Liu, Y. Lei, J. Tisdale, J. Baldwin, S. Xu, A. J. Neukirch, S. Tretiak, D. Vo, W. Nie, *ACS Appl. Mater. Interfaces* **2020**, *12*, 45533.

[29] a) J. Chen, Y. Fu, L. Samad, L. Dang, Y. Zhao, S. Shen, L. Guo, S. Jin, *Nano Lett.* **2017**, *17*, 460; b) Y. Wang, Z. Chen, F. Deschler, X. Sun, T.-M. Lu, E. A. Wertz, J.-M. Hu, J. Shi, *ACS Nano* **2017**, *11*, 3355.